Interplay between Thermally Induced Aragonite–Calcite Transformation and Multistep Dehydration in a Seawater Spiral Shell (*Euplica Scripta*)

Taiga Tone and Nobuyoshi Koga*

Department of Science Education, Division of Educational Sciences, Graduate School of Humanities and Social Sciences, Hiroshima University, 1-1-1 Kagamiyama, Higashi-Hiroshima 739-8524, Japan.

Contents

* Correspondence: nkoga@hiroshima-u.ac.jp; Tel.: +81-82-424-7092

S1. Sample characterization

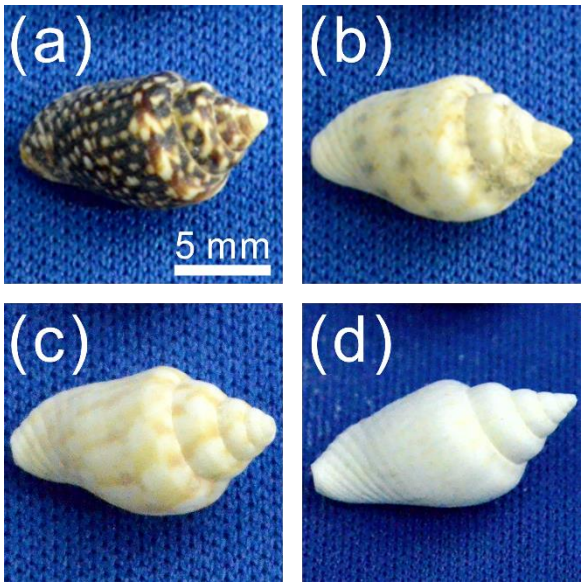

Figure S1. Appearance of the shell samples in different color groups: (a) brown, (b) light brown, (c) beige, and (d) white.

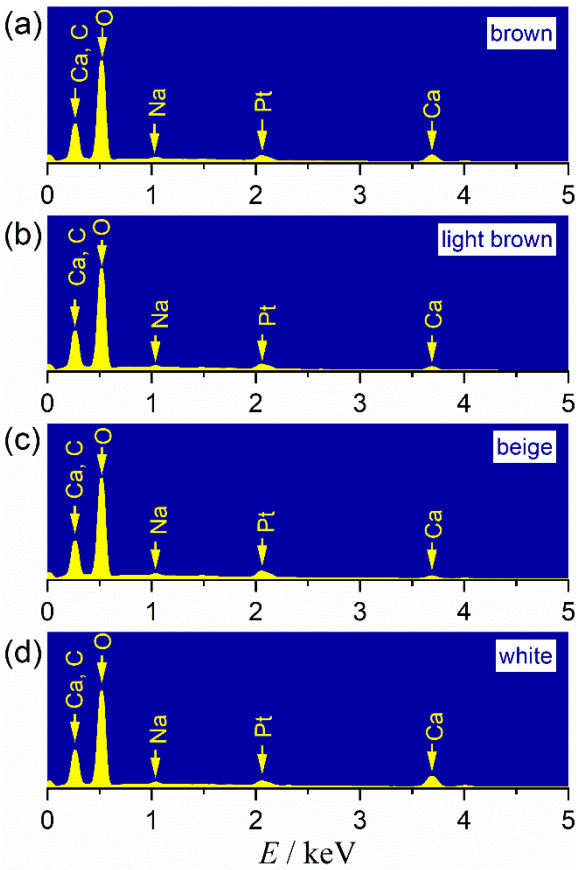

Figure S2. EDX spectra of the shell powder samples: (a) brown, (b) light brown, (c) beige, and (d) white.

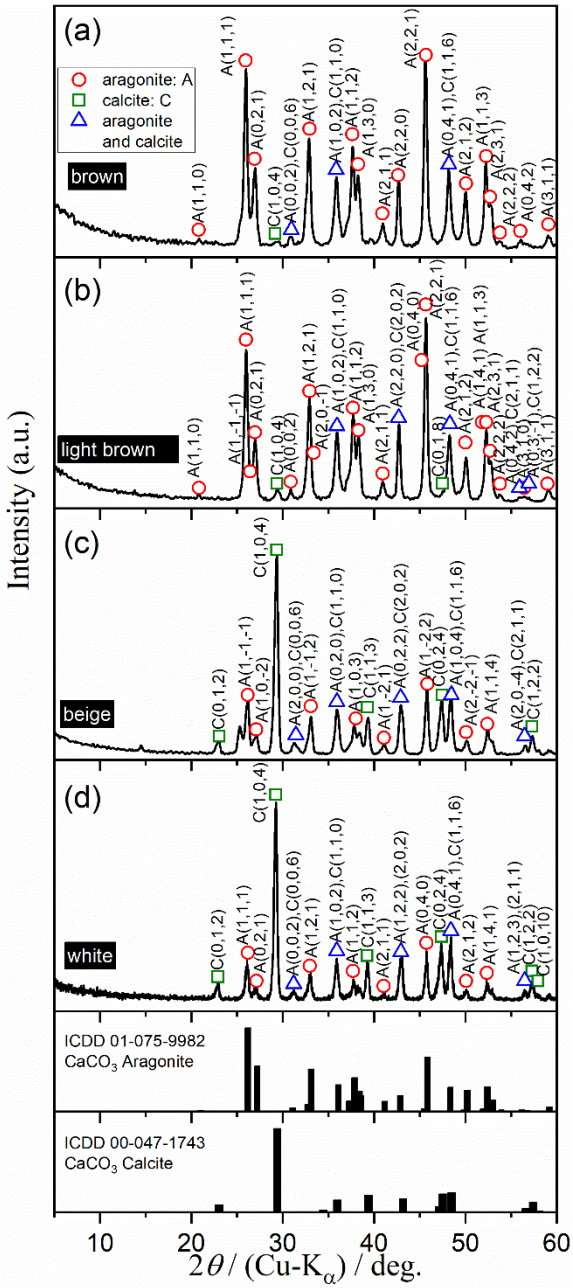

Figure S3. XRD patterns of the shell powder samples in different color groups: (a) brown, (b) light brown, (c) beige, and (d) white.

Table S1. Content ratio of aragonite in different shell powder samples determined from XRD patterns and FT-IR spectra

shell powder sample	Content ratio of aragonite / wt%	
	XRD	FT-IR
brown	95.3	95.7
light brown	93.5	94.7
beige	58.2	55.9
white	57.9	54.2

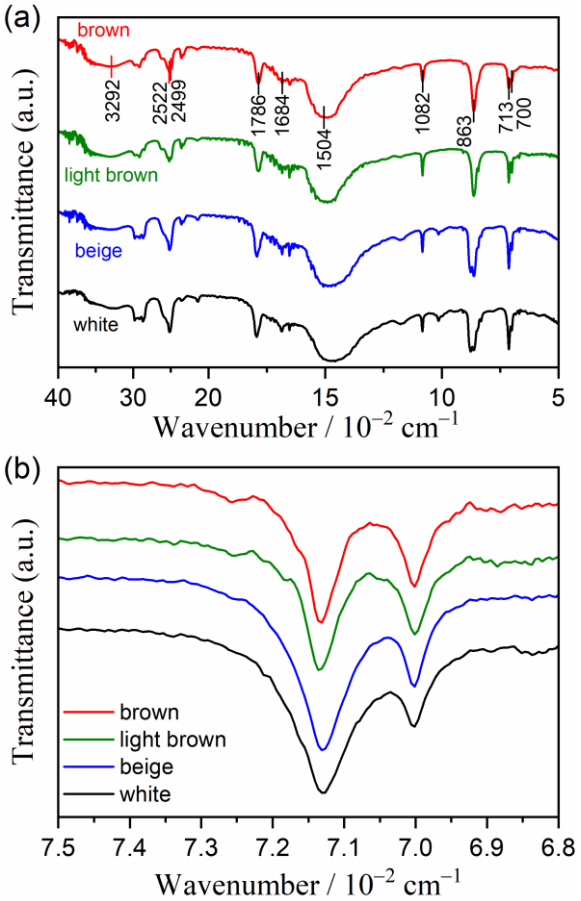

Figure S4. FT-IR spectra of the shell powder samples: (a) overview and (b) absorption peaks of the ν_4 mode of CO_3^{2-}.

The FT-IR spectra were converted to absorption spectra using the Kubelka–Munk conversion (Figure S5(a)). The specific double peaks with maxima at 700 and 713 cm^{-1} were deconvoluted into two separated peaks using the Lorentzian function.

$$y = a_0 \Big/ \left[1 + \left(\frac{x - a_1}{a_2}\right)^2\right], \qquad \text{(S1)}$$

where a_0–a_2 are the amplitude, center, and width (>0), respectively. From the result of the peak deconvolution, the peak areas of each separated peak were obtained. The area of the peak with maximum at 700 cm^{-1}, attributed to aragonite, was denoted as S_1. The area of the peak with maximum at 713 cm^{-1} was the sum of the peak areas attributed to aragonite (S_2) and calcite (S_3).

The peak area fractions of the peaks with maxima at 700 and 713 cm^{-1}, f_1 and f_2, respectively, were expressed as follows:

$$f_1 = \frac{S_1}{S_1 + S_2 + S_3} \quad \text{and} \quad f_2 = \frac{S_2 + S_3}{S_1 + S_2 + S_3} \qquad \text{(S2)}$$

The peak area fraction (f_3) attributed to calcite was expressed as follows:

$$f_3 = \frac{S_3}{S_1 + S_2 + S_3} = \frac{S_2 + S_3}{S_1 + S_2 + S_3} - \frac{S_2}{S_1 + S_2 + S_3} \qquad \text{(S3)}$$

The peak area, S_2, was calculated from the ratio of S_1 and S_2 in the pure aragonite sample. From the FT-IR spectra of the standard samples with various known content ratios of aragonite and calcite, the relationship between the molar fraction of calcite and the f_3 value was established as the calibration curve (Figure S5(b)). The content ratio of aragonite and calcite was determined from the FT-IR spectra of the sample using the calibration curve.

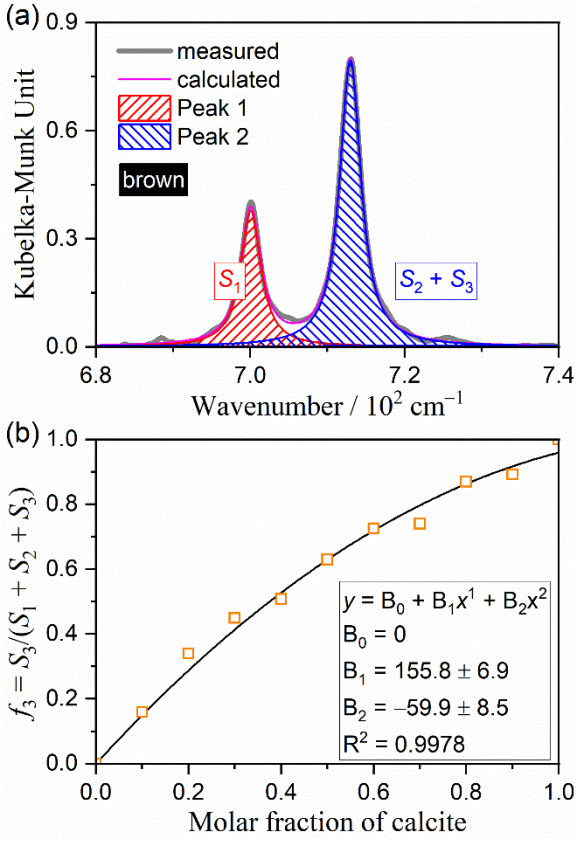

Figure S5. Determination of the content ratio of aragonite and calcite using the FT-IR spectra via the peak deconvolution and calibration curve methods: (a) an example of the deconvolution of the absorption peaks attributed to the ν_4 mode of CO_3^{2-} using the Lorentzian functions, and (b) calibration curve for determining the content ratio of calcite from the FT-IR spectrum of the sample

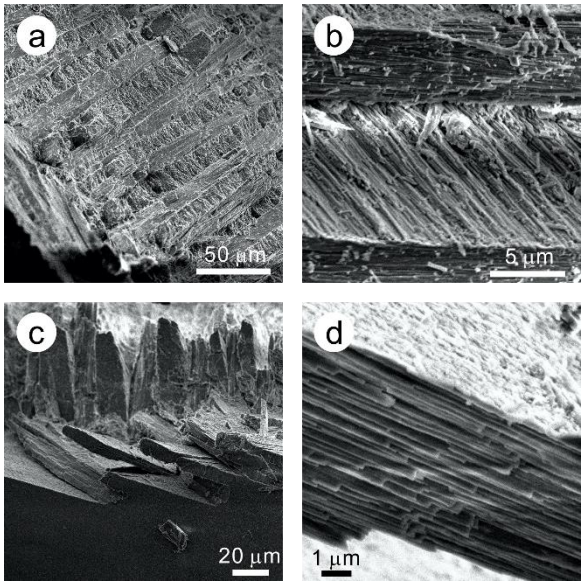

Figure S6. SEM images of the cross-sectional surfaces of the roughly crushed brown shell: (a) the first-order lamella of the middle layer, (b) second- and third-order lamellas of the middle layer, (c) first-order lamella of the inner layer, and (d) second- and third-order lamella of the inner layer.

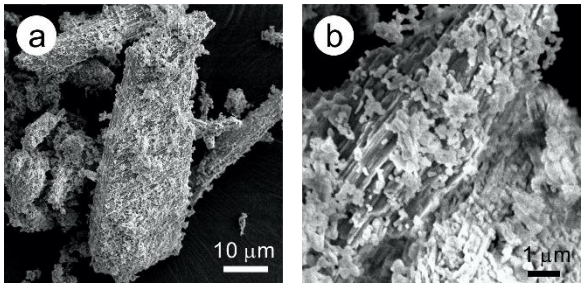

Figure S7. SEM images of the powdered brown shell with different magnifications: (a) ×1500 and (b) ×10000.

S2. Thermal behavior

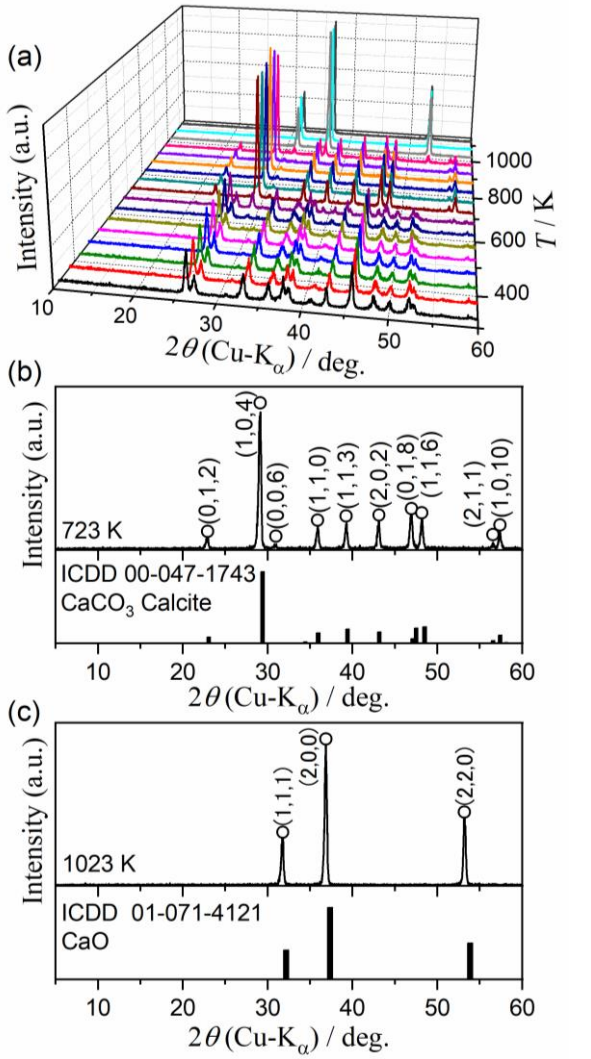

Figure S8. Changes in the XRD patterns during the heating the brown shell powder sample using the stepwise isothermal heating program in a stream of dry N_2 gas: (a) XRD patterns at different temperatures, (b) 723 K, and (c) 1023 K.

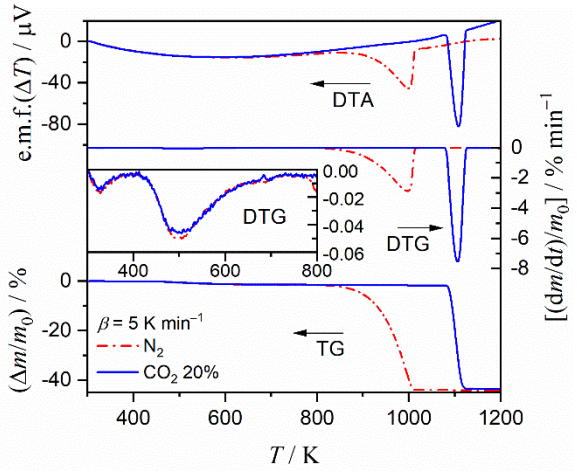

Figure S9. Comparison of TG–DTA curves for the brown shell powder sample (m_0 = approximately 20 mg) recorded at a β of 5 K min^{-1} in a stream of dry N_2 and N_2–CO_2 mixed (20%-CO_2) gases.

S3. Kinetics of the A–C transformation

Table S2. Kinetic model functions for solid-state reactions

kinetic model function	$g(\alpha)$
Phase boundary controlled; R(n) (n = 1, 2, and 3)	$1-(1-\alpha)^{\frac{1}{n}}$
One-dimensional diffusion controlled; D(1)	α^2
Two-dimensional diffusion controlled; D(2)	$\alpha+(1-\alpha)\ln(1-\alpha)$
Three-dimensional diffusion controlled (Jander eq.); D(3)	$\left[1-(1-\alpha)^{\frac{1}{3}}\right]^2$
Three-dimensional diffusion controlled (Ginstling-Brounshtein eq.); D(4)	$1-\frac{2}{3}\alpha-(1-\alpha)^{\frac{2}{3}}$
First order; F(1)	$-\ln(1-\alpha)$
Nucleation-Growth; JMA(m) (m = 0.5, 1.5, 2, 2.5, 3, and 4)	$[-\ln(1-\alpha)]^{\frac{1}{m}}$

Table S3. The rate constant k determined through a $g(\alpha)$ versus t plot using R(3) and F(1) functions

kinetic model function	T / K	k / s^{-1}	γ, [a]
F(1)	643	$(5.37 \pm 0.05) \times 10^{-5}$	0.9985
	653	$(1.11 \pm 0.03) \times 10^{-4}$	0.9968
	663	$(2.52 \pm 0.04) \times 10^{-4}$	0.9988
	673	$(5.52 \pm 0.11) \times 10^{-4}$	0.9992
R(3)	643	$(1.45 \pm 0.02) \times 10^{-5}$	0.9988
	653	$(2.91 \pm 0.05) \times 10^{-5}$	0.9976
	663	$(6.43 \pm 0.16) \times 10^{-5}$	0.9974
	673	$(1.38 \pm 0.04) \times 10^{-4}$	0.9986

[a] Correlation coefficient of the linear regression analysis of the $g(\alpha)$ versus t plot.

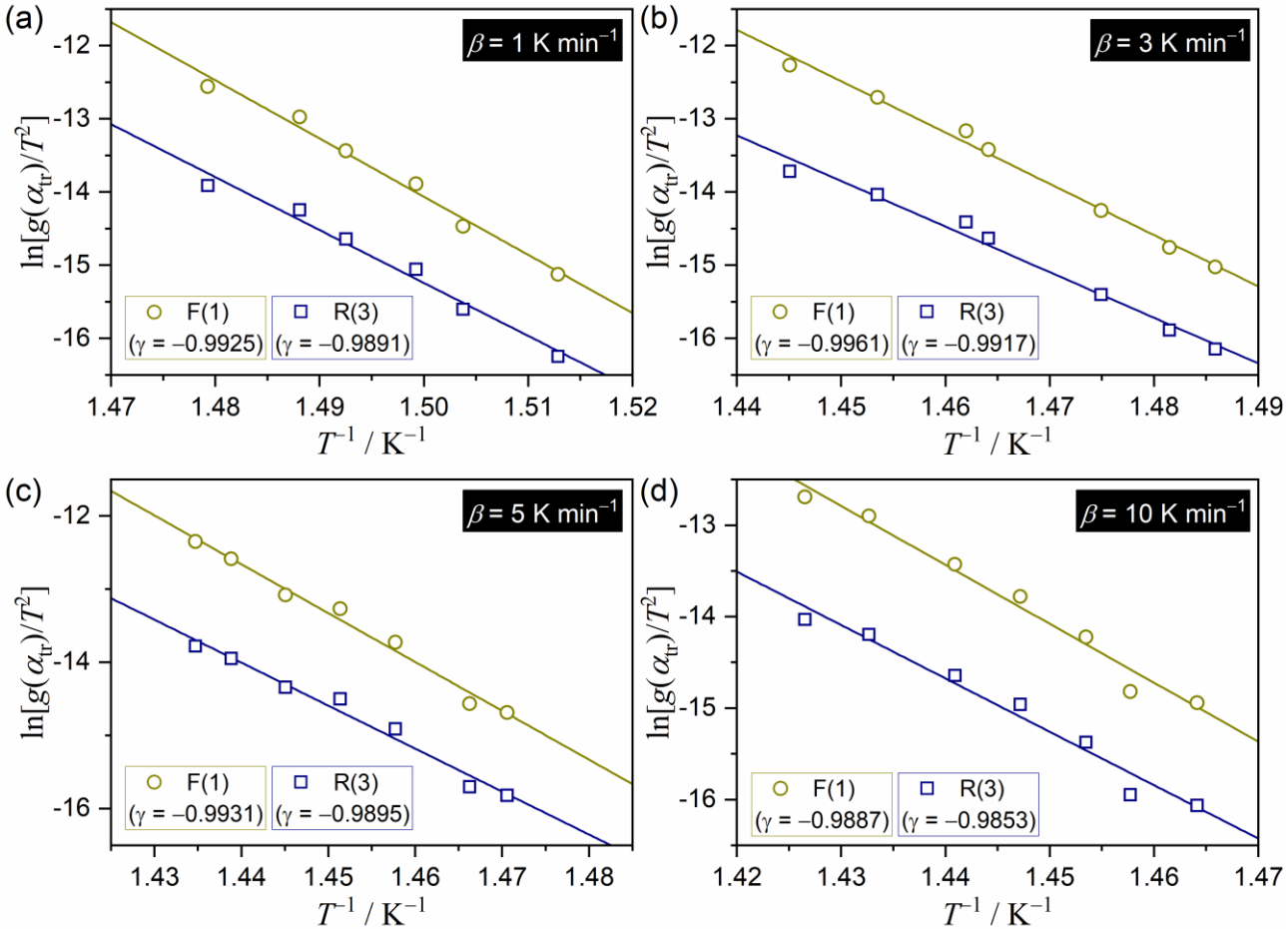

Figure S10. The Coats and Redfern plots based on the F(1) and R(3) models for the A–C transformation under nonisothermal conditions at different β values: (a) 1, (b) 3, (c) 5, and (d) 10 K min^{-1}.

Table S4. The Arrhenius parameters for the A–C transformation under linear nonisothermal conditions at different β values, determined using the Coats & Redfern method assuming the F(1) and R(3) models

kinetic model function	β / K min^{-1}	$E_{a,tr}$ / kJ mol^{-1}	ln(A_{tr} / s^{-1})	$-\gamma$ [a]
F(1)	1	661.2 ± 40.5	105.2 ± 7.3	0.9925
	3	583.0 ± 23.1	89.2 ± 4.1	0.9961
	5	555.0 ± 29.2	83.5 ± 5.1	0.9931
	10	535.6 ± 36.3	79.3 ± 6.4	0.9887
R(3)	1	601.3 ± 44.8	93.2 ± 8.1	0.9891
	3	518.2 ± 29.9	76.5 ± 5.3	0.9917
	5	488.3 ± 31.8	70.6 ± 5.6	0.9895
	10	485.3 ± 37.6	69.4 ± 6.6	0.9853

[a] Correlation coefficient of the linear regression analysis of the Coats & Redfern plot.

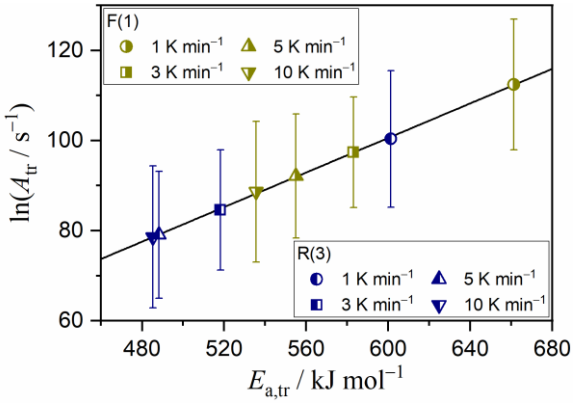

Figure S11. Linear correlation between the ln A_{tr} and $E_{a,tr}$ values determined for the A–C transformation under linear nonisothermal conditions using the Coats & Redfern method.

S4. Kinetics of the multistep thermal dehydration

S4-1. Formal kinetic analysis

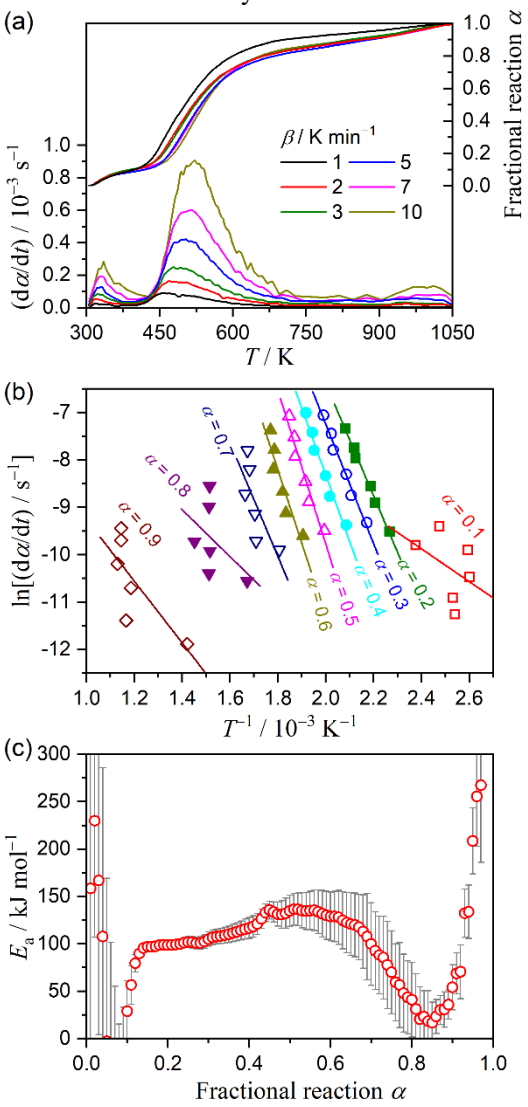

Figure S12. Results of the formal kinetic analysis based on the isoconversional kinetic relationship for the multistep thermal dehydration: (a) kinetic curves at different β values, (b) Friedman plots at different overall α values, and (c) E_a values at different overall α values.

S4-2. Mathematical deconvolution analysis

For the mathematical deconvolution analysis (MDA) for the three-step process of the thermal dehydration, various functions were examined to select a suitable one. The logistic power peak (LPP) function was selected as it provided the most statistically significant fit to the experimental DTG curves.

Figure S13 shows the typical MDA result using the LPP functions. The results provided rough estimates of the contributions of each reaction step to be (c_1, c_2, c_3) = (0.09, 0.78, 0.12) (Table S5). Simultaneously, a series of kinetic curves for each reaction step at different β values were obtained from the separated DTG curves (Figure S14). The kinetic curves were subjected to the Friedman plot (Figure S15). Although the Friedman plots exhibited a statistically significant linear correlation at each α_i value, irrespective of the reaction step (Figure S15), the slope systematically varied as the reaction advanced. The variation trends in the $E_{a,i}$ values were characteristic in each reaction step (Figure S16). In the first reaction step, the $E_{a,1}$ value systematically decreased with an increase in the α_1 value. Oppositely, the $E_{a,2}$ and $E_{a,3}$ values increased with an increase in the α_2 and α_3 values, respectively. Although these variations in the $E_{a,i}$ values as the reaction advanced were an indication of a complex kinetic feature that was not described as the ideal single step reaction, the α_i range with an approximately constant $E_{a,i}$ value could be selected. The average $E_{a,i}$ value was used to draw the experimental master plots for each reaction step according to the analogous kinetic equation used for the A–C transformation (eq. (6)). Figure S17 shows the experimental master plots of ($d\alpha_i/d\theta_i$) versus α_i for each reaction step of the thermal dehydration. Irrespective of the reaction step, the experimental master plot exhibited deceleration with concave shape, which was indicative of the diffusion-controlled process constrained by contracting geometry of the reaction interface. The experimental master plots were fitted with an SB(m, n, p) model (eq. (7)), obtaining the A_i values and the kinetic exponents in SB(m_i, n_i, p_i), as listed in Table S5.

$$F(t) = \frac{a_0}{a_3}\left[1 + \exp\left(\frac{t + a_2 \ln a_3 - a_1}{a_2}\right)\right]^{\frac{-a_3-1}{a_3}} \exp\left(\frac{t + a_2 \ln a_3 - a_1}{a_2}\right)(a_3 + 1)^{\frac{a_3+1}{a_3}}, \quad \text{(S4)}$$

where a_0–a_3 are the amplitude, center, width ($\neq 0$), and width (≥ 1), respectively.

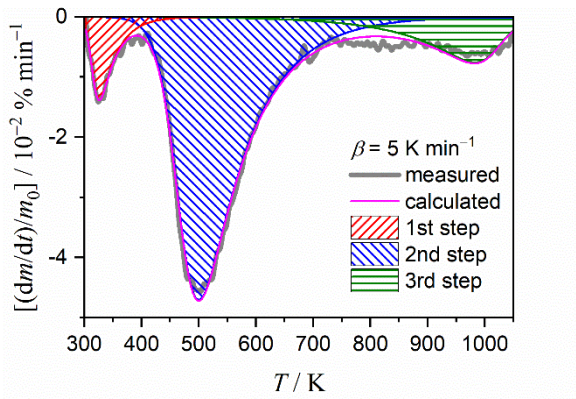

Figure S13. Typical MDA result using the LPP functions for the multistep thermal dehydration.

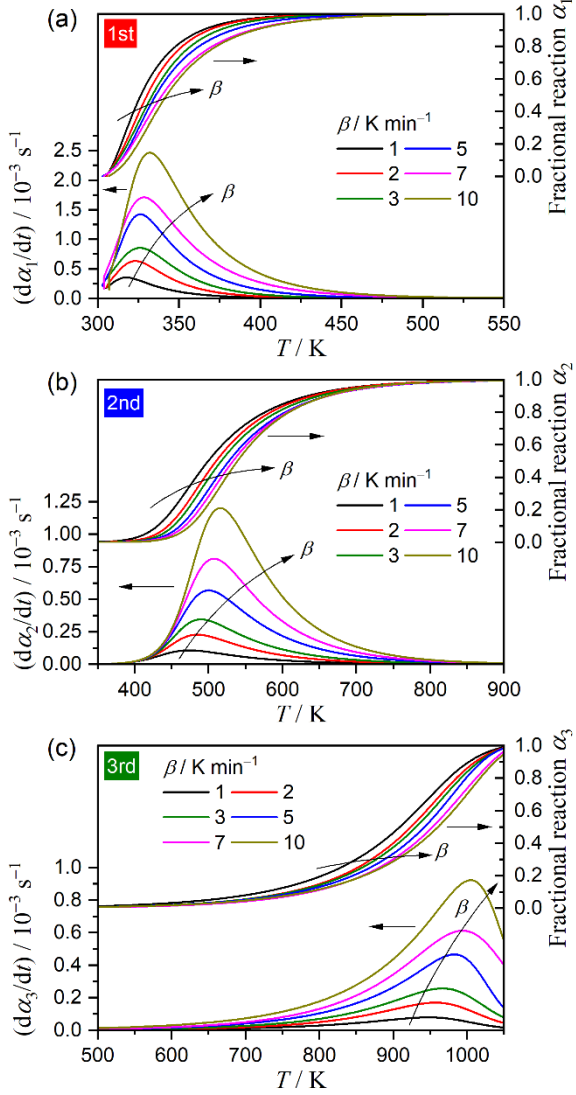

Figure S14. Kinetic curves at different β values for each reaction step of the multistep thermal dehydration, obtained using mathematically separated DTG curves: (a) the first, (b) second, and (c) third reaction steps.

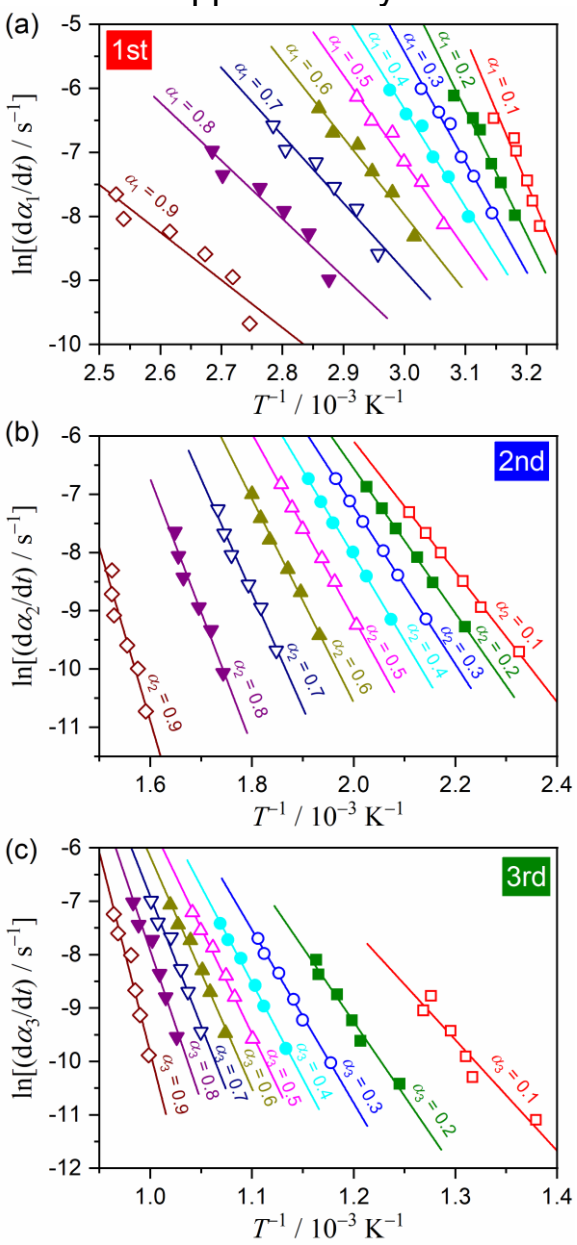

Figure S15. Friedman plots at different α_i values for each reaction step of the multistep thermal dehydration: (a) the first, (b) second, and (c) third reaction steps.

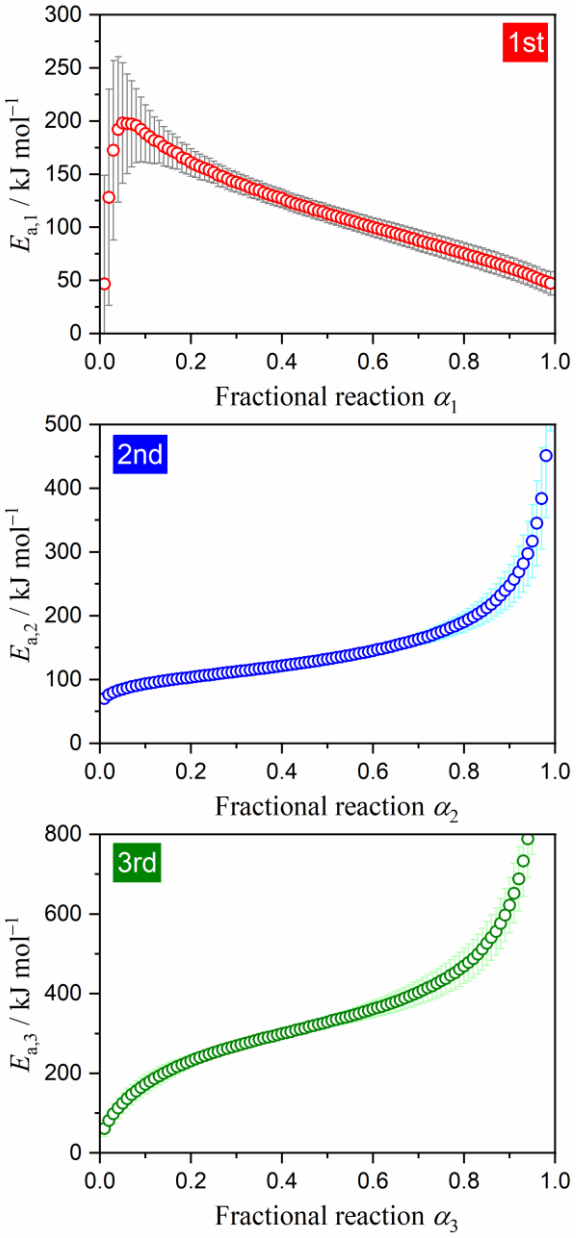

Figure S16. $E_{a,i}$ values at different α_i values for each reaction step of the multistep thermal dehydration: (a) the first, (b) second, and (c) third reaction steps.

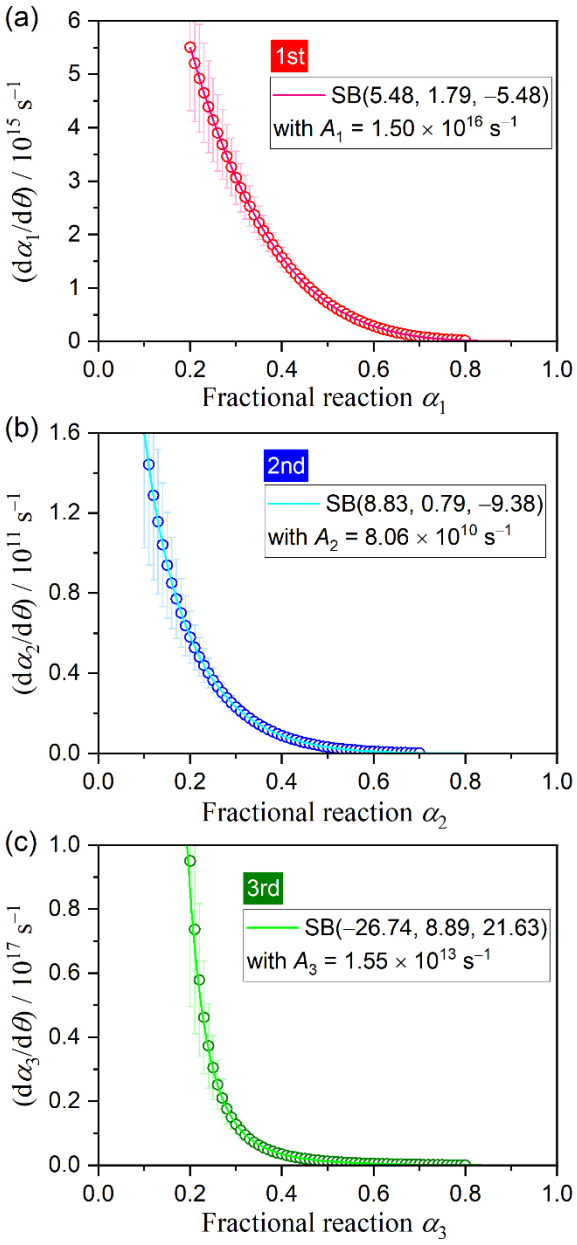

Figure S17. Experimental master plots of $(d\alpha_i/d\theta_i)$ versus α_i for each reaction step of the multistep thermal dehydration and fitting curve using SB(m_i, n_i, p_i): (a) the first, (b) second, and (c) third reaction steps.

Table S5. Kinetic parameters for each reaction step of the multistep thermal dehydration, obtained via the formal kinetic analysis of the mathematically separated kinetic curves

i	c_i	$E_{a,i}$ / kJ mol^{-1} (averaged range)	$\mathbf{d\alpha_i/d\theta_i = A_i\alpha_i^{m_i}(1-\alpha_i)^{n_i}[-\ln(1-\alpha_i)]^{p_i}}$				
			A_i / s^{-1}	m_i	n_i	p_i	R^{2,a}
1	0.09 ± 0.02	114.6 ± 24.7 ($0.2 \le \alpha_1 \le 0.8$)	(1.50 ± 0.01) × 10^{16}	5.48 ± 0.09	1.79 ± 0.04	−5.48 ± 0.09	> 0.9999
2	0.78 ± 0.04	128.8 ± 17.1 ($0.1 \le \alpha_2 \le 0.7$)	(8.06 ± 0.05) × 10^{10}	8.83 ± 0.24	0.79 ± 0.11	−9.38 ± 0.24	> 0.9999
3	0.12 ± 0.03	335.0 ± 63.5 ($0.2 \le \alpha_3 \le 0.8$)	(1.55 ± 0.14) × 10^{13}	−26.74 ± 3.13	8.89 ± 1.34	21.63 ± 3.00	> 0.9998

[a] Determination coefficient of nonlinear least squares analysis for fitting the master plot.